JOURNAL OF SPACECRAFT AND ROCKETS
Vol. 34, No. 5, September–October 1997

Damped Gyroscopic Modes of Spinning Tethered Space Vehicles with Flexible Booms

F. R. Vigneron* and A. M. Jablonski†
Canadian Space Agency, Saint-Hubert, Quebec J3Y 8Y9, Canada
R. Chandrashaker‡
Pratt and Whitney Canada, Longueuil, Quebec J4G 1A1, Canada
and
G. Tyc§
Bristol Aerospace, Ltd., Winnipeg, Manitoba R3C 2S4, Canada

The OEDIPUS rocket payload configuration comprises two spinning subpayloads, each having long flexible booms and a common long connecting tether of about 1 km in length. An analysis demonstrates the damped gyroscopic natural modes as a means of understanding the dynamics and stability of these very complex configurations. For OEDIPUS-A, attention is focused on calculation of nutation mode divergence that is attributable to material damping of the tether and booms. Calculated divergence rates are compared with flight data of OEDIPUS-A. For OEDIPUS-C attention is focused on attitude and configuration stability. It is noted to be stable in nutation and other modes at its flight spin rate of about 0.09 Hz. However, the configuration is noted to be susceptible to structural instability at spin rates above 0.26 Hz.

Nomenclature

A, B, C	= moments of inertia of end body, booms, and tether mass effects, kg-m^2
$\boldsymbol{A}, \boldsymbol{B}$	= constant system matrices of first-order form of model
A_0, B_0, C_0	= moments of inertia of inner rigid end body about O, kg-m^2
b	= distance between rotation point of end body and tether attachment (Fig. 2b), m
C_{b1}, C_{b2}	= material linear viscous damping coefficient of booms
C_t	= material linear viscous damping coefficient for tether
$\boldsymbol{D}$	= symmetric damping matrix of configuration
EI	= stiffness of booms, N-m^2
E_1, E_2	= matrix functionals in stiffness matrices of booms
$\boldsymbol{G}$	= skew-symmetric gyroscopic stiffness matrix
$\boldsymbol{K}$	= stiffness matrix of configuration
K_T	= stiffness submatrix of tether, N-m
K_1, K_2	= stiffness submatrices of booms, N-m
ℓ	= length of tether, m
ℓ_1, ℓ_2	= length of booms (Fig. 2c), m
$\boldsymbol{M}$	= symmetric mass matrix of configuration
M_T	= tether mass submatrices, kg-m^2
M_1, M_2	= boom mass submatrices, kg-m^2
m, n	= order of discretization
O	= center of mass and of rotation of end body
$OX_1\,X_2\,X_3$	= inertial coordinate system
$Ox_1\,x_2\,x_3$	= coordinate system attached to rigid end body
P	= origin of tether reference system at attachment point of tether to end body when configuration is undeformed
$PY_1\,Y_2\,Y_3$	= tether coordinate system that rotates with end body
P_1, P_2	= column matrix functions of discretized booms [Eq. (6)], kg-m^2
$\boldsymbol{Q}_k$	= complex eigenvector
q_5, q_6, q_7, q_8	= coordinate function matrices of boom deformation
$q_5^s, q_6^s, q_7^a, q_8^a$	= symmetric and antisymmetric coordinate function matrices of booms
R	= column matrix functionals of the tether [Eq. (6)], kg-m^2
S	= spin rate, cps
s	= field point of tether or boom length, m
T	= tether tension, N
t	= time, s
$\boldsymbol{U}_k, \boldsymbol{V}_k$	= real and imaginary parts of $\boldsymbol{Q}_k$
$\boldsymbol{u}, u, v, w$	= tether deformation vector and components (Fig. 2a), m
w_i	= boom deflection variables
$\boldsymbol{x}$	= state variable matrix for model in second-order form
$\boldsymbol{Z}$	= state variable matrix for model in first-order form
α_k, ν_k	= real and imaginary part of eigenvalue, 1/s
α_N, α_t	= real part of eigenvalue of nutation mode and tether modes, respectively, 1/s
ζ	= material damping ratios of tether or booms
θ, ψ, ϕ	= Euler angles of lower end body (Fig. 2b), deg
λ_k	= complex eigenvalue
ξ	= dimensionless length of tether or booms
ρ, ρ_1, ρ_2	= density per unit length of tether and booms, kg/m
Φ	= column matrix of assumed shape functions, tether or booms
ω	= fundamental cantilever frequency of booms, cps

Received Aug. 29, 1996; revision received May 8, 1997; accepted for publication May 9, 1997.

*Consultant, Space Technology Branch, 6767 Route de l'aeroport. Senior Member AIAA.
†Research Scientist, Space Technology Branch, 6767 Route de l'aeroport. Member AIAA.
‡Senior Engineer, Dynamics and Component Engineering. Member AIAA.
§Project Engineer, Special Projects Group. Member AIAA.

Introduction

THIS work was part of the OEDIPUS-A and C suborbital science missions and tether technology experiment.[1,2] The configuration of the OEDIPUS payloads is shown in Fig. 1. The main physical parameters are given in Table 1.

OEDIPUS-A was launched in 1989 into a suborbital trajectory of maximum altitude of 550 km with a three-stage Black Brant X rocket. The payload comprised two spinning subpayloads, each

Table 1 Parameters of OEDIPUS configurations

Parameter	OEDIPUS-A Forward payload	OEDIPUS-A Aft payload	OEDIPUS-C Forward payload	OEDIPUS-C Aft payload
		Central body		
C_0, kg-m^2	1.72	3.24	2.22	2.39
B_0, kg-m^2	24.1	36.6	32.5	14.7
A_0, kg-m^2	24.1	36.6	32.5	14.7
C_0/A_0	0.0714	0.089	0.068	0.163
C, kg-m^2	1.781	4.7564	155.35	51.39
B, kg-m^2	24.1	36.6	109.9	39.2
A, kg-m^2	24.1	38.116	109.9	39.2
C/A	0.0737	0.1248	1.4135	1.31
S, Hz	0.71	0.71	0.09	0.09
		Booms		
ℓ_1, m	0.88	2.57	9.0	6.5
ℓ_2, m	0.0	0.0	9.0	6.5
EI, N-m^2	3750	57.4	116.2	116.2
ρ_1, kg/m	0.367	0.134	0.134	0.134
ρ_2, kg/m	0.0	0.0	0.134	0.134
ω, Hz	73.04	1.7535	0.2	0.39
ζ, %	5	10	5	5
		Tether		
T, N	0–1.1	0–1.1	0–1.5	0–1.5
b, m	0.78	0.78	0.74	0.65
ℓ, m	958	958	1170	1170
ρ, kg/m	0.00297	0.00297	0.00297	0.00297
ζ, %	5	5	5	5

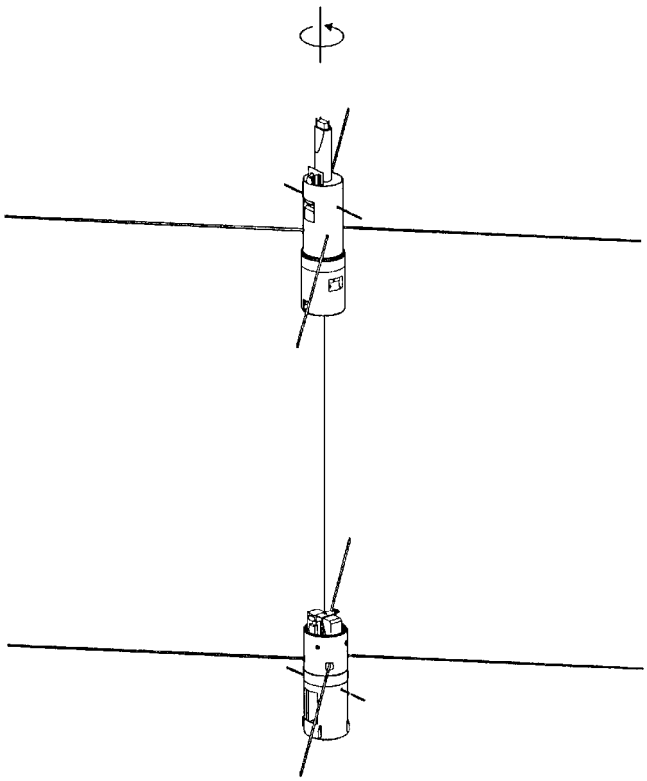

Fig. 1 Configuration of OEDIPUS payloads.

having two flexible deployable booms, and a common long connecting tether. During launch, the subpayloads were joined and were ejected from the launch vehicle with a spin rate about their longitudinal axis. The booms were then deployed, and shortly after, the spinning subpayloads were separated by a cold gas system. The subpayloads with booms deployed were minor-axis spinners. During separation, the tether deployed to a length of 958 m while its tension was held constant at about 1.1 N by magnetic hysteresis brake on the deployment reel. The dynamics of the forward payload was as expected prior to launch; it maintained its minor-axis spin and a small tip-off nutation at a constant value for 700 s following separation. The aft payload, however, experienced an unexpected anomaly; its initial small tip-off nutation diverged to about 35 deg over the 700 s, although preflight analysis had predicted a negligible divergence.[3] Computer simulations with a model comprising a subpayload, flexible booms, and the tether interaction modeled as a forcing term on the subpayload showed that the tether was the possible source of the nutation divergence. A later model that included a flexible tether[4] supported this finding, although the results were still not fully conclusive.

OEDIPUS-C comprised a science mission and payload configuration similar to that of the earlier OEDIPUS-A mission. Because of the flight anomaly of OEDIPUS-A, extensive dynamic modeling and analysis were done to provide a base for confident design of OEDIPUS-C.[4,5] Key aspects of the modeling were validated by ground tests.[6,7] Based on the knowledge gained, the subpayloads of OEDIPUS-C were configured to be dynamically stable major-axis spinners by providing each with four long booms.[8] OEDIPUS-C was launched in November 1995. During flight, the booms were deployed prior to subpayload separation, and the tether was deployed to a length of 1200 m. Each subpayload maintained stable major-axis spin throughout 960 s of suborbit without divergence of nutation, as planned.

Because the configuration of space vehicles is very complex, an understanding of the interrelationships between dynamic stability and the various parameters is not straightforward. The use of computer simulation and stability criteria from linear theory, as described in Ref. 4, for example, does not provide adequate insight into the dynamics and stability phenomena and into all possibilities.

In this paper, the merits of analyses of the damped gyroscopic natural modes of the configuration are demonstrated. The results contribute to a thorough understanding of the relative roles of the tether, booms, inner rigid bodies, and spin rate for OEDIPUS-A and OEDIPUS-C, respectively.

The subpayloads of OEDIPUS-A are minor-axis spinners (both with and without flexible booms) and are connected by a long tether. The modal analysis focuses on understanding the influence of flexibility and damping of the subcomponents (booms and tether) and the rate of divergence of the nutation of the subpayloads. Also, analytical results are compared with flight data.

The inner rigid bodies of the OEDIPUS-C are minor axis spinners, but the composite subpayloads are major-axis spinners by virtue of the four flexible booms. The modal analysis describes the basic stability of OEDIPUS-C and also shows the conditions for which the configuration has structural dynamic instability.

Mathematical Model

Modeling of the OEDIPUS configuration is described in earlier publications.[3–5,7] The main modeling objective is to understand the nutational and flexural dynamics of the end bodies (subpayloads) and the coupled lateral vibrations of the tether. As the tether is very long (up to 1.2 km) relative to the dimensions of the end bodies, the nutational dynamics of one end body does not significantly transmit or couple to the other end body. The longitudinal motions of the configuration are uncoupled from the end-body nutation at the level of linear modeling. The motion of the system may be approximated by a weighted sum of two types of modes: the first type derived from analysis of the tether and forward end body, and the second type derived from the tether and aft end body.

The linear equations of a spinning end body with booms and connected tether are documented fully in Ref. 5. The variables that describe the deformed state are shown in Figs. 2a–2c. The upper end of the tether at $s = \ell$ is constrained to be on OX_3. The rigid inner hub of the end body is defined by a 3–2–1 Euler angle rotation sequence. For small nutation angles, θ and ψ define the motion of the spin axis and ϕ defines the spin angle. The deformation of the tether is defined relative to $[PY_1\ \ Y_2\ \ Y_3]$, which rotates with the spin angle of the lower body. The tether displacement has components $u(s, t)$, $v(s, t)$, and $w(s, t)$. The end body and tether are connected at point P and, hence, the Euler angles and tether coordinates are interrelated as follows:

$$u(0, t) = b\theta, \qquad v(0, t) = -b\psi \tag{1}$$

The tether deformations are discretized using assumed shape factors with the series

$$u(s,t) = (1-\xi)b\theta(t) + \ell\Phi^T(\xi)q_9(t)$$
$$v(s,t) = -(1-\xi)b\psi(t) + \ell\Phi^T(\xi)q_{10}(t) \tag{2}$$

In Eq. (2), $x = s/\ell$, ℓ is the length of the tether, Φ is a column matrix of assumed sinusoidal shape functions, and q_9 and q_{10} are column matrices of corresponding time-dependent deformation variables

$$\Phi(\xi) = \begin{bmatrix} \Phi_1(\xi) \\ \bullet \\ \bullet \\ \Phi_m(\xi) \end{bmatrix}$$
$$q_9(t) = \begin{bmatrix} q_{9,1}(t) \\ \bullet \\ \bullet \\ q_{9,m}(t) \end{bmatrix}, \qquad q_{10}(t) = \begin{bmatrix} q_{10,1}(t) \\ \bullet \\ \bullet \\ q_{10,m}(t) \end{bmatrix} \tag{3}$$

The assumed tether shapes are $\Phi_n(\xi) = \sin n\pi\xi/\ell$.

Continuum variables $w_i(s,t)$ that describe the two sets of booms of the end body are shown in Fig. 2c. The variables are discretized by

$$w_i(s,t) = \ell_1\Phi^T(\xi)q_i(t), \qquad i = 1,3,5,7$$
$$w_i(s,t) = \ell_2\Phi^T(\xi)q_i(t), \qquad i = 2,4,6,8 \tag{4}$$

The shape functions in this case contain the set of cantilever mode shapes of the booms. Because the sets of booms are symmetric about the spin axis, symmetric and antisymmetric coordinates are introduced to simplify the modeling. Specifically, q_5 and q_7 are replaced by

$$q_5^a = \tfrac{1}{2}(q_5+q_7), \qquad q_5^s = \tfrac{1}{2}(q_5-q_7)$$
$$q_6^a = \tfrac{1}{2}(q_6+q_8), \qquad q_6^s = \tfrac{1}{2}(q_6-q_8) \tag{5}$$

To obtain the mathematical model, the kinetic and potential energies of the flexible end body and tether are derived in terms of the continuum coordinates just noted and then are transformed to discrete variables via Eqs. (2–5). The potentials are then used in Lagrange's equations to derive a series of linear differential equations. The algebra involved is straightforward although lengthy.[5] The second-order matrix format is outlined as

$$\boldsymbol{M}\ddot{\boldsymbol{x}} + (\boldsymbol{D}+\boldsymbol{G})\dot{\boldsymbol{x}} + \boldsymbol{K}\boldsymbol{x} = \boldsymbol{0} \tag{6}$$

In Eq. (6), $\boldsymbol{x} = [\psi, \theta, q_6^{aT}, q_5^{aT}, q_9^T, q_{10}^T]^T$ is the state variable. It has order $n = 2 + m_{b1} + m_{b2} + m$, where m_{b1} and m_{b2} are the order of discretization of the boom sets and m is the order of discretization of the tether. The matrix coefficients are constant and are defined as

$$\boldsymbol{M} = \begin{bmatrix} A & 0 & 2P_2^T & 0 & 0 & -R^T \\ 0 & B & 0 & 2P_1^T & R^T & 0 \\ 2P_2 & 0 & 2M_2 & 0 & 0 & 0 \\ 0 & 2P_1 & 0 & 2M_1 & 0 & 0 \\ 0 & R & 0 & 0 & M_T & 0 \\ -R & 0 & 0 & 0 & 0 & M_T \end{bmatrix}$$

$$K = \begin{bmatrix} (C-B)S^2+bT & 0 & 2S^2P_2^T & 0 & 0 & S^2R^T \\ 0 & (C-A)S^2+bT & 0 & 2S^2P_1^T & -S^2R^T & 0 \\ 2S^2P_2 & 0 & 2(K_2+S^2E_2) & 0 & 0 & 0 \\ 0 & 2S^2P_1 & 0 & 2(K_1+S^2E_1) & 0 & 0 \\ 0 & -S^2R & 0 & 0 & K_T-S^2M_T & 0 \\ S^2R & 0 & 0 & 0 & 0 & K_T-S^2M_T \end{bmatrix}$$

$$\boldsymbol{D} = \begin{bmatrix} 0&0&0&0&0&0 \\ 0&0&0&0&0&0 \\ 0&0&2C_{b2}&0&0&0 \\ 0&0&0&2C_{b1}&0&0 \\ 0&0&0&0&C_T&0 \\ 0&0&0&0&0&C_T \end{bmatrix}, \qquad \boldsymbol{G} = \begin{bmatrix} 0 & -(A+B-C)S & 0&0 & -2SR^T & 0 \\ (A+B-C)S & 0 & 0&0 & 0 & -2SR^T \\ 0 & 0 & 0&0 & 0 & 0 \\ 0 & 0 & 0&0 & 0 & 0 \\ 2SR & 0 & 0&0 & 0 & -2SM_T \\ 0 & 2SR & 0&0 & 2SM_T & 0 \end{bmatrix}$$

The mass, damping, and stiffness matrices, $\boldsymbol{M}$, $\boldsymbol{D}$, and $\boldsymbol{K}$, respectively, are symmetric. The gyroscopic matrix $\boldsymbol{G}$ is skew symmetric. The equations thus define a linear, vibratory, damped gyroscopic system. The elements within the matrices are further defined as

$$A = A_0 + \frac{2}{3}\rho_2\ell_2^3 + \frac{1}{3}\rho\ell b^2, \qquad B = B_0 + \frac{2}{3}\rho_1\ell_1^3 + \frac{1}{3}\rho\ell b^2$$
$$C = C_0 + \frac{2}{3}\rho_2\ell_2^3 + \frac{2}{3}\rho_1\ell_1^3$$
$$K_T = T\ell\int_0^1 \Phi_\xi\Phi_\xi^T\,d\xi, \qquad R = \rho\ell^2 b\int_0^1 (1-\xi)\Phi\,d\xi$$
$$M_T = \rho\ell^3\int_0^1 \Phi\Phi^T\,d\xi$$
$$P_1 = \rho_1\ell_1^3\int_0^1 \xi\Phi\,d\xi, \qquad P_2 = \rho_2\ell_2^3\int_0^1 \xi\Phi\,d\xi$$
$$M_1 = \rho_1\ell_1^3\int_0^1 \Phi\Phi^T\,d\xi, \qquad M_2 = \rho_2\ell_2^3\int_0^1 \Phi\Phi^T\,d\xi$$
$$K_1 = \frac{EI}{\ell_1}\int_0^1 \Phi_{\xi\xi}\Phi_{\xi\xi}^T\,d\xi, \qquad K_2 = \frac{EI}{\ell_2}\int_0^1 \Phi_{\xi\xi}\Phi_{\xi\xi}^T\,d\xi$$
$$E_1 = \frac{1}{2}\rho_1\ell_1^3\int_0^1 (1-\xi^2)\Phi_\xi\Phi_\xi^T\,d\xi$$
$$E_2 = \frac{1}{2}\rho_2\ell_2^3\int_0^1 (1-\xi^2)\Phi_\xi\Phi_\xi^T\,d\xi$$

The coefficient C_t represents assumed linear viscous material damping of the tether. The coefficients C_{b1} and C_{b2} represent assumed linear viscous damping of the booms.

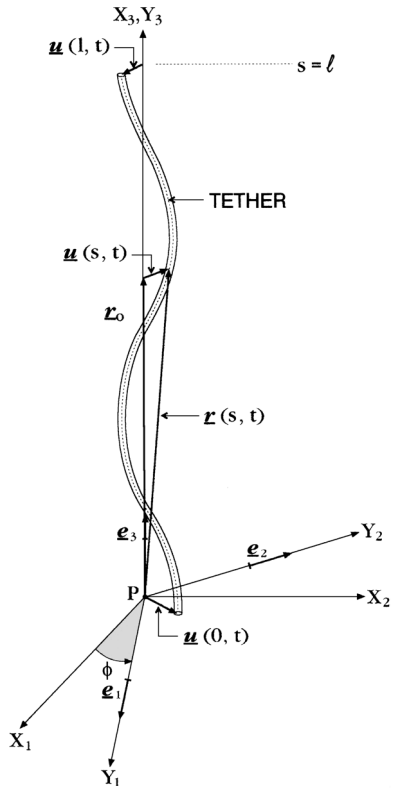

Fig. 2a Continuum variables of the tether.

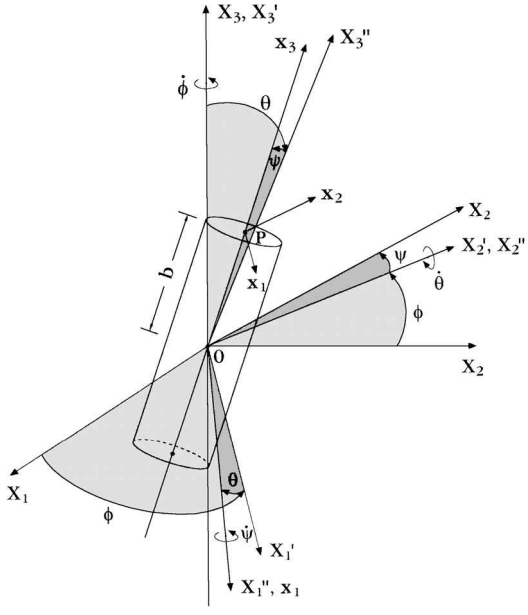

Fig. 2b Euler angles of end body and connection point *P* of tether.

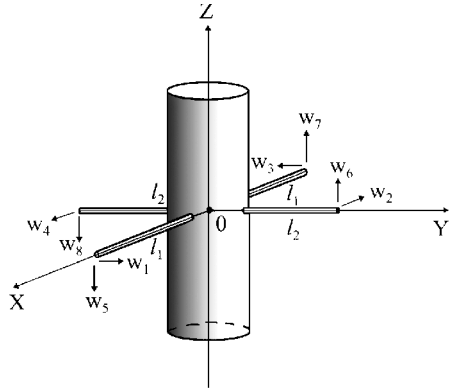

Fig. 2c Continuum variables of booms.

Real-valued damped gyroscopic natural modes and frequencies may be derived from Eq. (6) using the methods of Ref. 9. Equation (6) may be rearranged in the following form:

$$\boldsymbol{A}\dot{\boldsymbol{Z}} + \boldsymbol{B}\boldsymbol{Z} = \boldsymbol{0} \tag{7}$$

where

$$\boldsymbol{Z} = \begin{bmatrix} \dot{\boldsymbol{x}} \\ \boldsymbol{x} \end{bmatrix}, \qquad \boldsymbol{A} = \begin{bmatrix} \boldsymbol{M} & \boldsymbol{0} \\ \boldsymbol{0} & \boldsymbol{K} \end{bmatrix}$$

$$\boldsymbol{B} = \begin{bmatrix} \boldsymbol{D} & \boldsymbol{0} \\ \boldsymbol{0} & \boldsymbol{0} \end{bmatrix} + \begin{bmatrix} \boldsymbol{G} & \boldsymbol{K} \\ -\boldsymbol{K} & \boldsymbol{0} \end{bmatrix}$$

$\boldsymbol{A}$ is symmetric and positive definite and has dimension $2n$, and $\boldsymbol{B}$ is the sum of a skew symmetric and a symmetric part and has dimension $2n$. For this structure of equation, the eigenproblem has $2n$ eigenvalues that are in conjugate pairs[9]:

$$\lambda_k = \alpha_k + i\nu_k, \qquad \lambda_k^* = \alpha_k - i\nu_k \tag{8}$$

The ν_k are the frequencies (damped) of the modes, and the α_k are proportional to the rate of convergence or divergence of the vibratory motions. Also, $2n$ corresponding eigenvectors occur in complex pairs and have the structure

$$\boldsymbol{Z}_k = \begin{bmatrix} \lambda_k \boldsymbol{Q}_k \\ \boldsymbol{Q}_k \end{bmatrix} \tag{9}$$

where $\boldsymbol{Q}_k = \boldsymbol{U}_k + i\boldsymbol{V}_k$ and $\boldsymbol{U}_k$ and $\boldsymbol{V}_k$ are real-valued parts of a complex eigenvector. The $\boldsymbol{Q}_k$ and λ_k are also solutions to the eigenvector problem expressed in second-order form:

$$\left\{\boldsymbol{M}\lambda_k^2 + (\boldsymbol{D} + \boldsymbol{G})\lambda_k + \boldsymbol{K}\right\}\boldsymbol{Q}_k = \boldsymbol{0} \tag{10}$$

A real-valued eigenvector $\boldsymbol{x}_k$ that satisfies Eq. (10) is

$$\boldsymbol{x}_k = \tfrac{1}{2}\left(\boldsymbol{Q}_k e^{\lambda_k t} + \boldsymbol{Q}_k^* e^{\lambda_k^* t}\right) \tag{11}$$

This is real valued, due to the pairing of complex and complex-conjugate quantities. It further reduces to the following form, which is the damped gyroscopic mode shape expressed in real-valued quantities:

$$\boldsymbol{x}_k = e^{\alpha_k t}\{\boldsymbol{U}_k \cos \nu_k t - \boldsymbol{V}_k \sin \boldsymbol{\nu}_k t\} \tag{12}$$

Computer software has been written to solve the eigenvalue problem to yield modal frequencies, modal convergence/divergence, i.e., growth/decay, ratios, and time-varying mode shapes, for given input parameters (inertias of the end bodies, spin rate, mass, stiffness damping, and length of the booms, and mass, damping tension, and length of the tether). Equation (12) is the basis for the computer-generated animation of the mode shapes.[10] The mode shapes associated with a particular ν_k and its counterpart $-\nu_k$ are linearly dependent, and in processing of computed data it is necessary to be consistent when choosing which modes to retain. In this work the set designated as linearly independent are the modes with {negative α_k, positive ν_k} and {positive α_k, negative ν_k}. This convention provides for interpretation of motions in terms of forward or backward gyroscopic precessions as is done for rotating machinery.[11]

OEDIPUS-A

The parameters of OEDIPUS-A are given in Table 1. The forward and aft subpayloads are minor-axis spinners in the flight configuration with the flexible booms deployed. The subpayloads of OEDIPUS-A have two booms, whereas OEDIPUS-C has four booms.

Modal Analysis of OEDIPUS-A

The modal frequencies and corresponding real parts are plotted vs deploying tether length in Fig. 3 for the OEDIPUS-A aft payload. The discretization of the tether and booms is 9 and 3, respectively, and accordingly there are 23 modes in total. Analysis of this and other data and animation shows that the modes may be classified into four categories as labeled in Fig. 3: one nutation mode, where

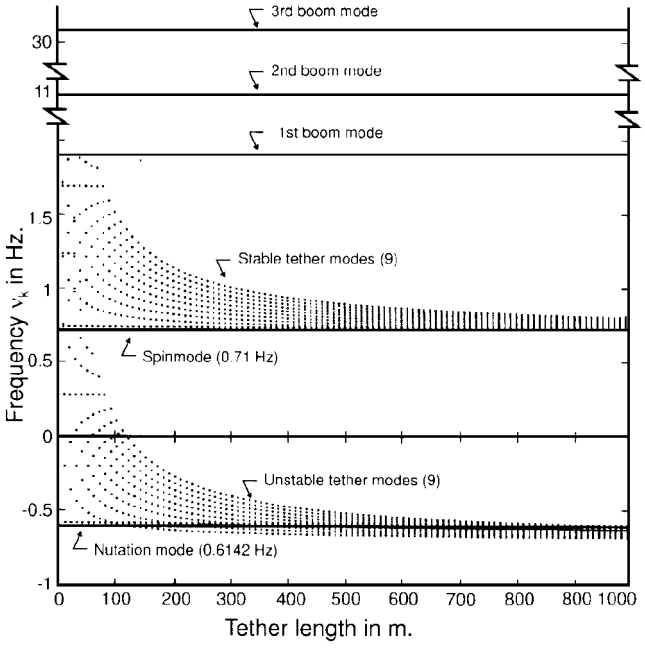

a) ν_k

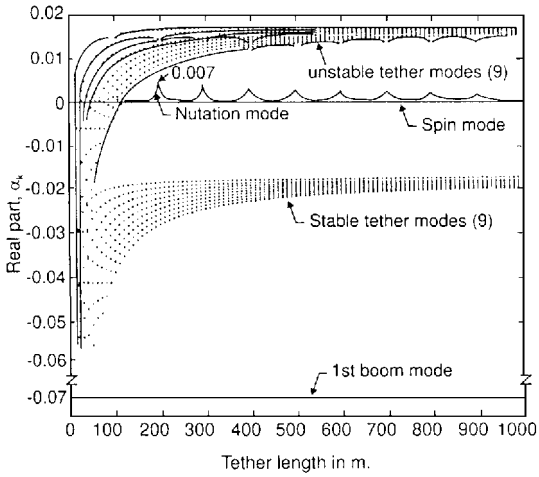

b) α_k

Fig. 3 Eigenvalues vs tether length for OEDIPUS-A aft payload.

the motion is essentially rigid body nutation with additional small subresonant boom and tether deformation; one spin mode, where the configuration rotates as a rigid body about the spin axis; tether modes, where the main motions are vibration modes of the tether, accompanied by a very small end-body rocking and boom flexure; and boom modes, where the motions are boom vibration, accompanied by rocking of the end body.

The real parts of the eigenvalues corresponding to nutation and tether modes will be designated by the symbols α_N and α_t, respectively. The following observations are noted in Fig. 3.

1) The frequencies of the nutation, spin, and boom modes are almost constant for all tether lengths. This indicates that the tether, which is very light, does not influence the frequencies of the end body.

2) The frequency of the nutation mode is about 0.6196 Hz. The calculated rigid body nutation frequency $\sqrt{[(C-A)(C-B/AB]S}$ is 0.6143 Hz. The frequency of the spin mode is 0.716 Hz, whereas $S = 0.71$ Hz. Thus, the tether and boom flexibility alter the rigid end-body frequencies by less than 1%.

3) The nutation mode α_N is positive and, therefore, the mode is unstable. This is in accord with the minor-axis spinner stability rule.

4) There are 18 tether modes, and their frequencies decrease with deployed length, as expected from a simple fixed-end string model. At tether lengths of less than about 10 m, all of the tether frequencies are positive and the corresponding α are negative, indicating that all

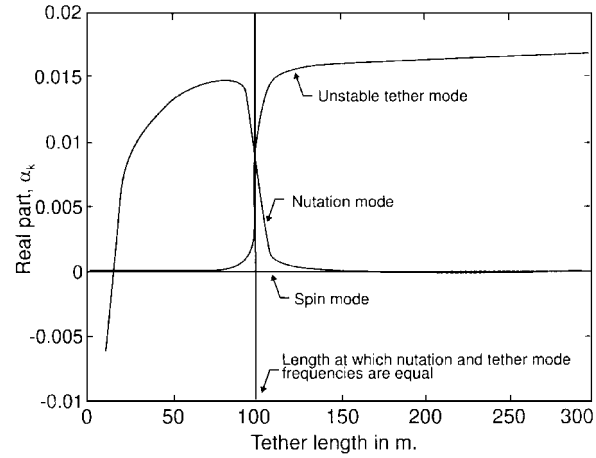

Fig. 4 Eigenvalue α_k vs tether length for discretization of 1 for tether and booms.

of the modes are stable. At about $\ell = 10$ m, the frequency of the lowest tether mode is zero, and the corresponding α changes from negative to positive; thus the mode is unstable for tether lengths beyond 10 m.

5) At beyond 120 m of deployed tether length, 9 of the 18 tether modes are unstable and 9 are stable. The stable frequencies asymptote to the spin frequency.

6) The frequencies of the three boom modes are above 1.9 Hz. They are well separated from the other 20 modes. The corresponding α are negative, which indicates stability.

7) In Fig. 3, the α_N of the nutation mode is positive and varies in an arch fashion with peaks. The peaks occur at lengths where a tether mode frequency intersects with the nutation mode. This important feature is amplified further in the following.

To understand the interaction between a tether mode and the nutation mode, data were calculated with the tether discretized with one assumed coordinate function. The α_k vs length for the nutation and tether modes is shown in Fig. 4. (The calculation also included a boom set discretized with order one, but the boom modes are omitted from the graph to make it less confusing.) The tether mode and nutation mode couple where their frequencies are close, causing an increase by orders of magnitude in the divergence rate of nutation.

The results have been corroborated to an extent in laboratory experiments.[6,7] Regarding unstable tether modes, although linear theory indicates that they are unstable, in laboratory tests they are evidenced as resonant, bounded motions and are stabilized by nonlinear forces that are omitted in the linear model. Nutation convergence or divergence is determined by the sign of α_N; tether modes do not destabilize the end body because they are essentially stabilized by nonlinear tension forces and their mass is small relative to the inertia of the end body.

The mechanisms of growth of the nutation mode are of particular interest because during flight OEDIPUS-A experienced an unexpected nutation angle divergence of the aft payload. Figures 5–7 provide more insight into this aspect.

Figure 5 shows the α_N vs spin rate for a constant tether length. Thus, the interaction between nutation and tether modes depends on spin frequency.

Figure 6 shows results comparable to Fig. 5 but with the tether absent from the model. The α_N is due only to boom damping and is very small (order of 10^{-5}) relative to values with the tether present (order 10^{-4}–10^{-3}; Fig. 5). Thus, the tether is the main quantitative contributor to nutation mode divergence.

Figure 7 shows α_N vs the material damping coefficient of the tether, for a case where the tether and booms are discretized at orders 9 and 3, respectively. The input damping ratio of the component tether is believed to be in the range of 5%, and the graph shows that uncertainty in this value could affect α_N by a factor of two or more. Computer runs of the equivalent of Fig. 5 were done with 20 assumed tether functions (as opposed to 9). The increased number does not change the basic shape of α_N, but the peaks and troughs rise by about 10%. Computer runs were also done at various tension levels,

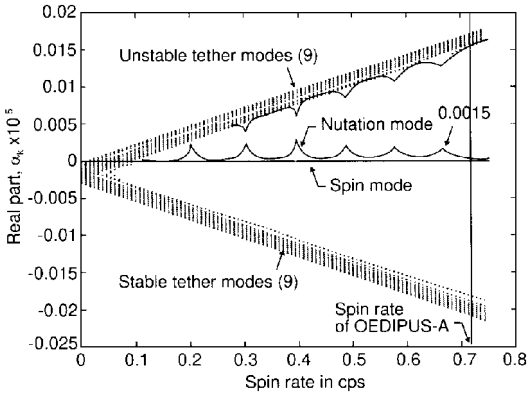

Fig. 5 Eigenvalue α_N vs spin rate for constant tether length, OEDIPUS-A aft payload.

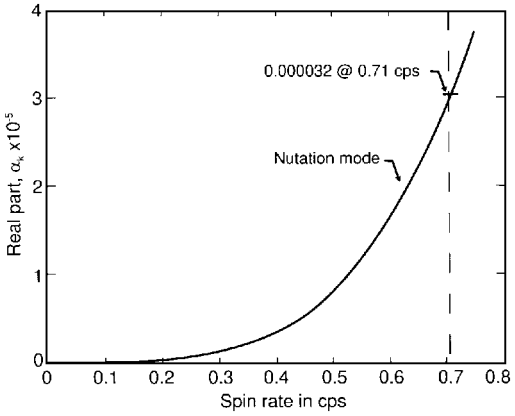

Fig. 6 Eigenvalue α_N vs spin rate, tether absent; divergence due to boom damping only.

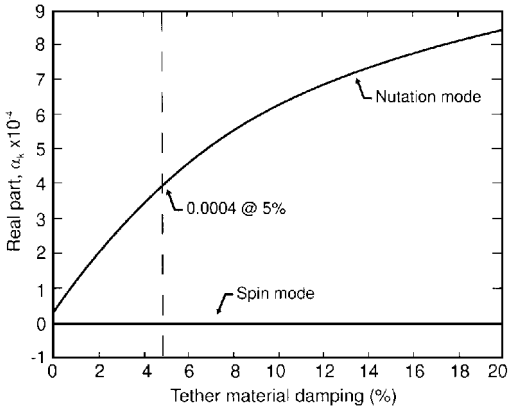

Fig. 7 Eigenvalue α_k for nutation and spin modes vs tether material damping; tether and booms discretization order of 9 and 3, respectively.

from 1.1 to 0.25 N. The α_N acquires many more peaks because lower tensions result in more tether frequencies that interact with nutation. Overall, the peaks are lower and α_N is less by a factor of about 2 at low tensions.

Comparison of Flight Data with Calculated Results

The flight performance of OEDIPUS-A is described in Ref. 3.

Aft Payload

Figure 8 presents the nutation time history of the aft payload as deduced from the magnetometer data of the flight. A curve fit of $\theta_0 e^{\alpha(t-t_0)}$ to the data yields the values of α summarized in Table 2. An analytic equation for $\theta(t)$ that is based on the superposition of modes is

$$\theta(t) = \sum_{k=1}^{n} \theta_k e^{\alpha_k t} \left\{ U_k^\theta \cos \nu_k t - V_k^\theta \sin \nu_k t \right\} \qquad (13)$$

Table 2 Nutation divergence coefficients from flight data of OEDIPUS-A

Time segment, s	α	Comment
200–450	0.0052	Tether deploying, $T = 1.1$ N
450–650	0.0031	Tether deployed, $T = 0.1$–0.4 N

Table 3 Comparison of calculated α_N with flight-derived values

	Deploying $\ell = 200$ m $T = 1.1$ N	Deployed $\ell = 958$ m T about 0.1 N
Linear model		
Peak	0.007	0.002
Trough	0.0005	0.001
Approximate mean	0.003	0.001
Flight data	0.005	0.003

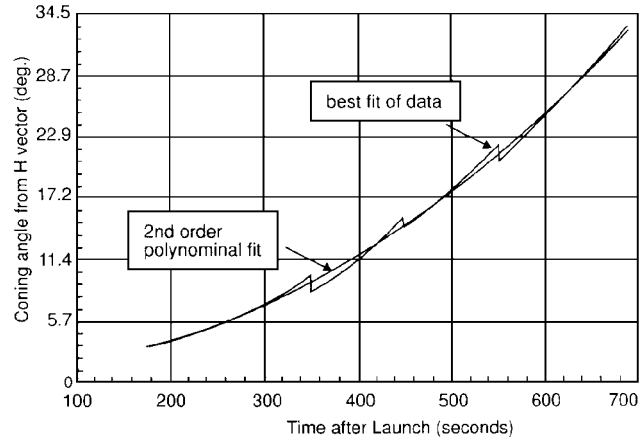

Fig. 8 OEDIPUS-A aft payload divergence rate as deduced from flight magnetometer data.

where U_k^θ and V_k^θ are components of the eigenvectors. As the nutation mode is distinct and essentially uncoupled in shape from the other modes, it follows that a reasonable analytic approximation for $\theta(t)$ is given by truncation of the preceding series at one mode, namely, the nutation mode. It follows that the calculated α_N of the nutation mode is essentially the equivalent of the flight-derived α of Table 2.

Table 3 gives the range of calculated divergence rates, as derived from Fig. 3 and similar additional data. The flight data are included for comparison. Table 3 indicates agreement between flight data and linear model calculations to within a factor of 2–3. The agreement could be adjusted favorably by assuming a higher tether material damping or by changing other uncertain parameters. Also, a damping model other than linear viscous might result in a closer match. Overall, the agreement may be considered very good, relative to the state of the art in modeling and substructure synthesis of structural damping.

Forward Payload

Flight data of the forward payload show that the nutation angle did not diverge to any significant extent, i.e., the flight-derived α was near zero for the forward payload of OEDIPUS-A. The forward payload inertias and tether parameters are similar to those of the aft payload (Table 1), and the current analytical model yields an α_N that is similar to that of the aft payload, i.e., of the order of 10^{-3}. Hence, there is a mismatch between flight results and modeling for the forward payload.

The current model does not account for the tether deployment reel that is mounted on the forward payload, nor does it account for a large offset between the center of mass of the end body and the boom attachment location. Also, the two-stage booms did not fully deploy, and their flexibility properties are uncertain. It is suspected that the reel, which has an unmodeled rotational spring type of flexibility, may uncouple the tether from the forward payload. If modeled, it

might explain the mismatch. The topic remains for future analytical and laboratory investigation.

OEDIPUS-C

The parameters of OEDIPUS-C are given in Table 1. Each rigid inner subpayload is a minor-axis spinner. However, with the four flexible booms added, the configuration becomes a major-axis spinner.

Modal Analysis of OEDIPUS-C

The calculated modal parameters vs spin rate are shown in Fig. 9 for the representative spin rate and tension of $S = 0.09$ Hz and $T = 0.09$ N, respectively. The modal characteristics are noted to be similar to those of OEDIPUS-A (Fig. 3) as regards tether and boom modes and couplings and interactions with the end body. A freeze-frame from animation[10] of a damped gyroscopic mode shape is shown in Fig. 10. The following observations are of additional significance.

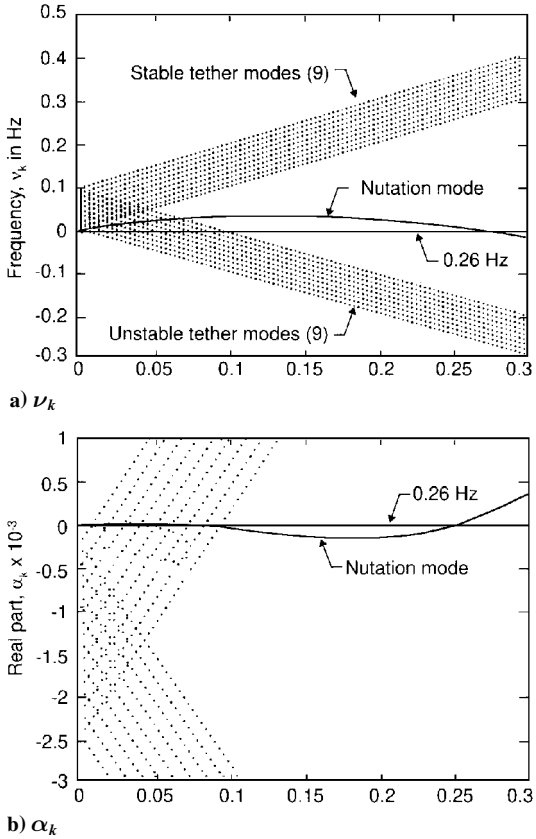

Fig. 9 Eigenvalues vs tether length for OEDIPUS-C forward payload; tension = 1.1 N, spin rate = 0.09 cps

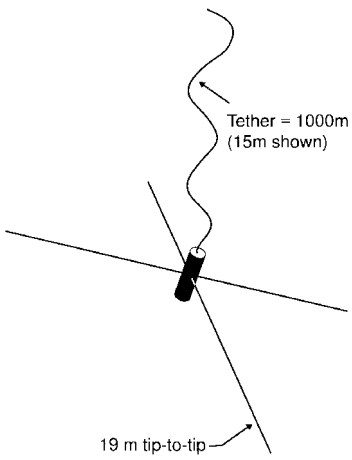

Fig. 10 Freeze frame of animation of damped gyroscopic natural mode.

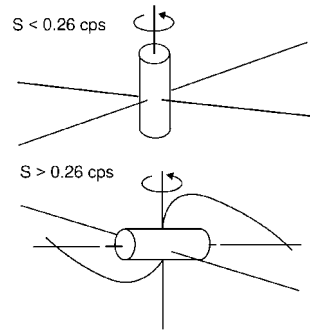

Fig. 11 Equilibrium configurations for OEDIPUS-C; spin rate was 0.084 cps during flight.

1) There are 9 tether modes below the flight spin rate of 0.09 Hz that have positive α, i.e., that are linearly unstable. As already discussed, on the basis of laboratory investigation, these modes may be expected to be stabilized by nonlinear tether tension related forces.

2) The remaining tether and boom modes have negative α and are thus stable.

3) The values of the nutation mode α_N are negative for the range 0–0.26 Hz, and for this range the nutation mode is stable. The spin rate of OEDIPUS-C at 0.09 Hz is well within the stable range.

4) At above 0.26 Hz, the nutation frequency is negative and the α_N abruptly changes sign to positive, which indicates instability.

The abrupt sign change is associated with a structural dynamic instability of the configuration. OEDIPUS-C is a major-axis spinner, and this particular instability is not forecast by the major-axis spin rule of energy sink theory. The structural instability is shown in Fig. 11. Above a spin rate of 0.26 Hz, the destabilizing gyroscopic torque of the inner rigid minor-axis spinner is greater than the stabilizing elastic resisting moments at the roots of the booms. The configuration seeks its lowest energy state, which is a deformed configuration, as shown schematically. The tether tension contributes to stability, but its mass and restoring moment are low and have only a minor effect on OEDIPUS parameters.

Flight of OEDIPUS-C

OEDIPUS-C was successfully flown in November of 1995. It was equipped with a video camera and a tether force sensor. An overview of the data is given in companion papers.[12,13] The configuration was observed to be stable as regards α_N and all of the other modes of forward and aft payloads. A future paper will report a comparison of the calculated modes with nutational and structural modes derived by fast Fourier transform processing of three-axis force sensor data of the flight.

Conclusions and Remarks

This work demonstrates dynamic characteristics of the OEDIPUS spinning tethered space vehicle that may be useful for the design of future space systems of like configuration.

The divergent nutation of the aft payload of OEDIPUS-A was caused by the tether. The boom flexibility was not a major factor. Earlier published results obtained through computer solution in the time domain are validated by the more complete understanding offered herein.

The nutation modes of the OEDIPUS-C payload are calculated to be stable for the nominal parameters of the mission. However, the configuration is susceptible to boom-associated structural instability at spin rates above 0.26 Hz.

Damped gyroscopic natural modes would be useful for understanding other spinning flexible configurations. The method enables categorization of the modes and analysis of their stability properties and their relative importance. A knowledge of natural modal properties is also essential for interpreting flight data of this type of system.

References

[1] James, H. G., and Tyc, G., "Flight Results from the OEDIPUS-A Tethered Experiment," *Proceedings of the 4th International Conference on Tethers in Space* (Washington, DC), Science and Technology, Hampton, VA, 1995, pp. 193–209.

[2]Eliuk, R., Walkty, I., Rob, R., Rumbold, G., and James, H. G., "OEDIPUS-C Tethered Suborbital Mission Description and Flight Performance," *Proceedings of the 9th CASI Conference on Astronautics*, Canadian Aeronautics and Space Inst., Ottawa, ON, Canada, 1996, pp. 332–341.

[3]Tyc, G., and Han, R. P. S., "Attitude Dynamics Investigation of the OEDIPUS-A Tethered Rocket Payload," *Journal of Spacecraft and Rockets*, Vol. 32, No. 1, 1995, pp. 133–141.

[4]Tyc, G., Han, R. P. S., Vigneron, F. R., Jablonski, A. M., Modi, V. J., and Misra, A. K., "Dynamics and Stability of Spinning Tethered Spacecraft with Flexible Appendages," *Advances in the Astrodynamical Sciences*, Vol. 85, Univelt, San Diego, CA, 1993, pp. 877–895 (AAS Paper 93-736).

[5]Vigneron, F. R., Jablonski, A. M., and Chandrashaker, R., "Tether Dynamics Model for the Tether Laboratory Demonstration System (TE-LAB)," Canadian Space Agency, CSA TR OED-TR-93-05, Rev. 1, Saint-Hubert, PQ, Canada, Nov. 1994.

[6]Modi, V. J., Pradhan, S., Chu, M., Tyc, G., and Misra, A. K., "Experimental Investigations of the Dynamics of Spinning Bodies," *Proceedings of the 4th International Conference on Tethers in Space* (Washington, DC), Science and Technology, Hampton, VA, 1995, pp. 1823–1836.

[7]Vigneron, F. R., Jablonski, A. M., Chandrashaker, R., Bergmans, J. L., McClure, B. A., and Tyc, G., "Comparison of Analytical Modeling of OEDIPUS Tethers with Data from Tether Laboratory," *Journal of Guidance, Control, and Dynamics*, Vol. 20, No. 3, 1997, pp. 471–478.

[8]Tyc, G., Vigneron, F. R., Jablonski, A. M., Chandrashaker, R., and Han, R. P. S., "Design of an Attitude Stabilization System for the OEDIPUS-C Tethered Rocket," *Proceedings of the 8th CASI Conference on Astronautics*, Canadian Astronautics and Space Inst., Ottawa, ON, Canada, 1994, pp. 313–322.

[9]Vigneron, F. R., "A Natural Modes Model and Modal Identities for Damped Linear Structures," *Journal of Applied Mechanics*, Vol. 53, March 1986, pp. 33–38.

[10]Chandrashaker, R., Vigneron, F. R., and Jablonski, A. M., "Computer Oriented 3-D Animation of the Tether Dynamics Model," *Proceedings of the 15th Canadian Conference on Applied Mechanics*, Vol. 2, Fleming Express Press, Victoria, BC, Canada, 1995, pp. 916, 917.

[11]Crandall, S. H., "Rotating and Reciprocating Machines," *Handbook of Engineering Mechanics*, 1st ed., McGraw–Hill, New York, 1962, pp. 58-20, 58-21.

[12]Tyc, G., Vigneron, F. R., Jablonski, A. M., Han, R. P. S., Modi, V. J., and Misra, A. K., "Flight Dynamics Results from the OEDIPUS-C Mission," *Proceedings of the AIAA/AAS Astrodynamics Conference* (San Diego, CA), AIAA, Reston, VA, 1996, pp. 39–56 (AIAA 96-3573).

[13]Jablonski, A. M., Vigneron, F. R., Rhew, R. D., Bergmans, J. L., Whitehead, W. R., and Tyc, G., "Preflight Testing and Flight Performance of the OEDIPUS-C Tether Force Sensor," *Journal of Spacecraft and Rockets*, Vol. 34, No. 4, 1997, pp. 533–541.

R. B. Malla
Associate Editor